International Journal of Multiphase Flow 141 (2021) 103568

Contents lists available at ScienceDirect

International Journal of Multiphase Flow

journal homepage: www.elsevier.com/locate/ijmulflow

A numerical approach to address the acoustic stiffness in cavitating flows

Mrugank Bhatt, Krishnan Mahesh*

Department of Aerospace Engineering and Mechanics, University of Minnesota, Minneapolis, MN 55455, USA

ARTICLE INFO

Article history:
Received 7 December 2020
Accepted 15 January 2021
Available online 24 February 2021

Keywords:
Preconditioning
Dual-time stepping
Compressible flows
Cavitation

ABSTRACT

A numerical approach based on preconditioning and dual-time stepping (*DTS*) is proposed to simulate cavitating flows at low Mach numbers. The methodology is based on a fully-compressible homogeneous mixture model and finite rate mass transfer as discussed in Gnanaskandan and Mahesh (2015). The method has shown promising results for capturing the large-scale cavitation in developed cavitation regimes (e.g. Bhatt and Mahesh, 2020; Gnanaskandan and Mahesh, 2016a). Small-scale vapor regions in the incipient cavitation, cavitation inception and wetted conditions are sensitive to free-stream nuclei content (e.g. Hsiao and Chahine, 2005; Bhatt and Mahesh, 2019, 2020). In these regimes, lower values of free-stream nuclei are necessary than what is typically prescribed in homogeneous mixture models that use a fully-compressible formulation. While important for the physical modeling, lower values of free-stream nuclei lead to acoustic stiffness. The goal of the present work is to present a numerical approach to enable such low free-stream nuclei calculations in an accurate manner and in a reasonable amount of time. The key aspects of the numerical approach are: (i) preconditioning applied to the cavitating flow equations in a fully-compressible (density-based) solver, (ii) modifications based on the all-speed Roe-type scheme to the characteristic-based filtering, and (iii) implementation in parallel and on unstructured grids that allow the simulation of complex problems. The numerical formulation of the time-derivative preconditioning matrix, the *DTS* framework, and modification to the shock-capturing are discussed. A proper conditioning of the preconditioned system of equations is obtained. The methodology is demonstrated for the unsteady flow over a cylinder under wetted and cavitation inception conditions, and LES of flow over a propeller under wetted conditions. Overall, a significant saving in total run-time as compared to the original solver is obtained, without compromising accuracy.

1. Introduction

Cavitation is the phase change of a liquid into vapor when the liquid pressure drops below vapor pressure. In many cavitation applications, it is essential to capture the propagation of acoustic waves and strong shock waves and therefore, the compressibility of the medium. The shock waves emitted by vapor cavity collapse are the major cause of noise, vibration, and material damage (Franc and Michel, 2006) in marine applications and rotating turbo-machinery. Bubbly shock wave propagation has been identified as an intrinsic mechanism behind sheet to cloud transition (Ganesh et al., 2016). In marine applications, acoustic waves are used as an indicator to detect cavitation inception. Numerical modeling of the compressibility in such problems poses a challenge due to the range of Mach numbers. It is known that the speed of the sound of a pure water can drop by orders of magnitude (e.g. from 1480 m/s to 10 m/s) with the addition of a gaseous phase and/or phase change. Fig. 1 shows a sharp decrease in the sound speed with the increase in the gaseous phase volume fraction starting from pure water. Hence, cavitating flows can be highly compressible despite the nearly incompressible nature of the water. In the present work, we propose a numerical approach based on preconditioning and dual-time stepping (*DTS*) to address the challenge posed by the range of Mach numbers. The goal of the present work is to extend a density-based solver that is generally robust at high Mach numbers to the low Mach number calculations in cavitating flows.

* Corresponding author.
E-mail address: kmahesh@umn.edu (K. Mahesh).

https://doi.org/10.1016/j.ijmultiphaseflow.2021.103568
0301-9322/

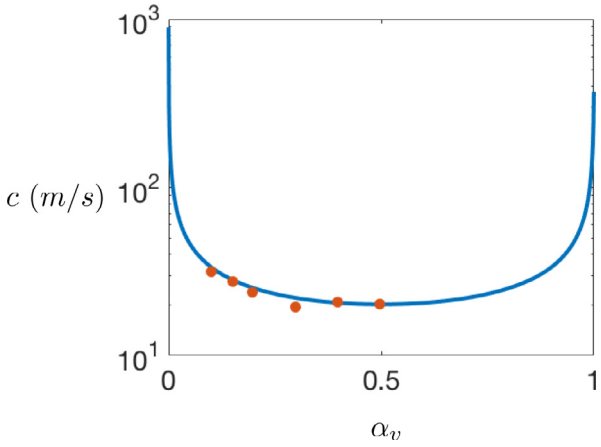

Fig. 1. Comparison of sound speed in water-gas mixture to experiments at 0.1 MPa. Current ▬, Karplus (1957) ●.

The most commonly used physical model to simulate cavitating flows is the homogeneous mixture model (Budich et al., 2018; Gnanaskandan and Mahesh, 2015; Bensow and Bark, 2010; Seo and Lele, 2009; Schnerr et al., 2008; Saito et al., 2007; Liu et al., 2004; Singhal et al., 2002; Ahuja et al., 2001; Kunz et al., 2000). The model treats the mixture of water and vapor as a single medium. One major difference between cavitation solvers based on the homogeneous mixture model is whether they use a pressure-based (e.g. Singhal et al., 2002) or a density-based algorithm (e.g. Seo and Lele, 2009); both of which have to address the range of Mach numbers in cavitating flows. Pressure-based algorithms proposed for single-phase flow often experience convergence problems due to the significant reduction in the speed of sound in the water-vapor mixture regions. Various modifications to pressure-based algorithms have been proposed to obtain the correct speed of sound in cavitating flows (e.g. Bensow and Bark, 2010; Senocak and Shyy, 2002; Singhal et al., 2002). On the other hand, density-based algorithms suffer from the accuracy and numerical stiffness due to nearly incompressible regions in water. To mitigate very low Mach numbers in water, several studies based on the fully-compressible formulation have used relatively high values of free-stream nuclei (Bhatt and Mahesh, 2020; Gnanaskandan and Mahesh, 2016a; 2016b; Seo and Lele, 2009; Saito et al., 2007) than typical free-stream nuclei concentrations measured in the experiments (e.g. Venning et al., 2018). Here, 'free-stream nuclei' refers to initial levels of vapor or non-condensable gases (*NCG*) present in the water. At sufficiently low pressures (typically the vapor pressure) these nuclei act as the starting point for the liquid to cavitate (Franc and Michel, 2006). The high values of free-stream nuclei reduce the speed of sound in the water and avoid extremely small time steps due to the acoustic stiffness.

Studies have shown that good agreement can be obtained with the experiments for capturing the large regions of vapor in the developed cavitation regimes (Bhatt and Mahesh, 2020; Gnanaskandan and Mahesh, 2016a; Saito et al., 2007) with high free-stream nuclei values. Although, wetted conditions, cavitation inception and incipient cavitation are highly sensitive to the free-stream nuclei content (Bhatt and Mahesh, 2019, 2020; Hsiao and Chahine, 2005). In such cases, lower values of free-stream nuclei consistent with the orders of magnitude observed in the experiments are necessary. For example, Bhatt and Mahesh (2020) studied partial cavitation over a range of regimes spanning the incipient to periodic shedding over a wedge. They obtained a very good comparison of the volume fraction data to the X-ray measurement of Ganesh et al. (2016) for the large regions of vapor in the developed cavitation regimes. However, in the incipient regime, they observed a noticeable difference in vapor void fraction compared to the experiments with the high values of free-stream nuclei. Bhatt and Mahesh (2019) showed that the propeller loads are sensitive to the choice of free-stream nuclei and the lower values are necessary for the accurate prediction of the propeller performance. Brandao et al. (2020) obtained experimentally consistent behavior of separation location over a range of regimes in the cylinder cavitation with the experimentally consistent values of the free-stream nuclei. The behavior was not captured with high free-stream nuclei content in the prior study of the same configuration (Gnanaskandan and Mahesh, 2016b). While important for physical modeling, lower values of free-stream nuclei impose a stringent requirement on the time step of the numerical method and affect the solution accuracy. Thus, for the density-based solvers, another approach is to retain the low free-stream nuclei and use preconditioning.

Preconditioning applied to the compressible flow equations slows the acoustic wave speed $(u + c)$ towards the fluid speed (u); thereby reducing the disparity in the eigenvalues. Preconditioning has provided a powerful remedy for the accuracy and convergence of compressible solvers at low Mach numbers (Guillard and Viozat, 1999; Hsu and Jameson, 2002; Kunz et al., 2000; LeMartelot et al., 2013; Li and Gu, 2008; Lindau et al., 2001; Merkle, 1998; Turkel, 1999; Vatsa and Turkel, 2003; Weiss and Smith, 1995). Many studies have made use of preconditioning for single-phase flows. A few studies also report algorithms for multiphase mixtures. Kunz et al. (2000) developed a preconditioning formulation in their two-fluid model using volume fraction as the dependent variable. The authors demonstrated efficient and accurate computations of various steady-state and transient sheet and super-cavity flows. However, in the formulation, they assumed constant densities in each phase and compressibility effects were not accounted for in the two-phase mixture region. Ahuja et al. (2001) developed a preconditioning algorithm accounting for the compressibility effects in the component phases and demonstrated results for steady-state flows. Lindau et al. (2001) discussed in detail the choice of preconditioning variables and the corresponding eigenvalues of the system for the homogeneous mixture model. Venkateswaran et al. (2002) presented the artificial compressibility based formulation for time-marching systems. They used perturbation theory to provide scaled preconditioning forms for the numerical computations. The algorithms use Jameson-type artificial dissipation term for the upwinding (Jameson, 1995) that is preconditioned as suggested in Turkel (1999). For density-based solvers, Hou and Mahesh (2005) demonstrated an approach to obtain the incompressible Navier–Stokes equation in the limit of low Mach by using the incompressible scaling for pressure in the compressible Navier–Stokes equations. Li and Gu (2008) proposed an all-speed Roe-type scheme and its asymptotic analysis of the low Mach behavior. They perform preconditioning of the Roe-type shock-capturing schemes by scaling the eigenvalues of the Jacobian matrix. LeMartelot et al. (2013) demonstrated the methodology to simulate liquid and liquid-gas flows at all-speeds. They extend the preconditioning variant of Guillard and Viozat (1999) for multi-phase flows that conserves energy and the phase transition is achieved in a thermodynamically consistent way.

In the present work, we extend the methodology of Gnanaskandan and Mahesh (2015) based on a compressible homogeneous mixture model to address the acoustic stiffness in cavitating flows. The method is parallel, unstructured and has shown promising results for the large scale cavitation in the developed cavitation regimes (e.g. Bhatt and Mahesh, 2020; Gnanaskandan and Mahesh, 2016a). The goal of the present work is to allow the methodology to simulate wetted conditions, incipient cavitation/cavitation inception calculations that typically require low free-stream nuclei, and consequently the solution

involving low Mach regions in the flow. We present a numerical approach based on the preconditioning and *DTS* to enable such calculations. The shock-capturing based on the characteristic-based filtering is modified by following the all-speed approach suggested by Li and Gu (2008) for Roe-type schemes. For constructing the time-derivate matrix, we use the strategies of pressure-based algorithms (e.g. Lindau et al., 2001). The current methodology differs from the prior studies on the preconditioning of multiphase homogeneous mixture system in the following ways; (i) the preconditioning that accomodates matrix dissipation in the shock capturing scheme alongside the traditional time-derivative preconditioning matrix, (ii) a use of fully-compressible formulation that uses a density-based solver (including compressible viscous fluxes), and (iii) use of conserved variables for physical time derivative and shock-capturing. The paper is organized as follows. The governing equations and the physical model is described in Section 2. The details of the preconditioning methodology are discussed in Section 3. The numerical experiments for the problems of interest are discussed in Section 4. Finally, the paper is summarized in Section 5.

2. Governing equations and physical model

We use the homogeneous mixture approach where the mixture of water and vapor is considered as a single compressible medium. We assume mechanical equilibrium (i.e. each phase has the same pressure as the cell pressure and slip velocity between the phases is not considered) and thermal equilibrium (i.e. temperature of each phase is the same as the cell temperature). Sub-grid scale bubble dynamics and surface tension effects are neglected. In hydrodynamic cavitation, the high specific heat capacity of the water, results in only minor temperature fluctuations. Hence, an isothermal formulation is used to reduce simulation time. Thus, the formulation somewhat differs from Gnanaskandan and Mahesh (2015), as the energy equation is not considered here. The governing equations are the compressible Navier–Stokes equations for the mixture quantities along with the transport equation for vapor mass fraction:

$$\begin{aligned}\frac{\partial \rho}{\partial t} &= -\frac{\partial}{\partial x_j}(\rho u_j),\\ \frac{\partial \rho u_i}{\partial t} &= -\frac{\partial}{\partial x_j}(\rho u_i u_j + p\delta_{ij} - \sigma_{ij}),\\ \frac{\partial \rho Y_v}{\partial t} &= -\frac{\partial}{\partial x_j}(\rho Y_v u_j) + S_e - S_c.\end{aligned} \tag{1}$$

Here ρ, u_i and p are density, velocity, and pressure of the mixture respectively, and Y_v is the vapor mass fraction. The mixture density is defined as

$$\rho = \rho_l(1-\alpha_v) + \rho_v\alpha_v, \tag{2}$$

where ρ_l and ρ_v are densities of liquid and vapor respectively, and α_v is the volume fraction of vapor. Volume fractions of each constituent phase are related to their respective mass fractions by

$$\rho_l(1-\alpha_v) = \rho(1-Y_v) \quad \text{and} \quad \rho_v\alpha_v = \rho Y_v. \tag{3}$$

The system is closed using a mixture equation of state obtained using a stiffened equation of state for the liquid, and ideal gas equation of state for vapor:

$$p = Y_v\rho R_v T + (1-Y_v)\rho K_l T\frac{p}{p+P_c}, \tag{4}$$

where $K_l = 2684.075$ J/(Kg K) and $P_c = 786.333\times10^6$ Pa are the constants associated with the equation of state for the liquid. The parameters were derived by Gnanaskandan and Mahesh (2015) to match speed of sound in liquid at a prescribed density to the NIST data. Gnanaskandan and Mahesh (2015) also validated the thermodynamic model for a variety of problems including sheet to cloud cavitation. $R_v = 461.6$ J/(Kg K) is the specific gas constant for equation of state of vapor obtained from Saito et al. (2007). The viscous stress tensor (σ_{ij}) is given by

$$\sigma_{ij} = \mu\left(\frac{\partial u_i}{\partial x_j} + \frac{\partial u_j}{\partial u_i} - \frac{2}{3}\frac{\partial u_k}{\partial x_k}\delta_{ij}\right), \tag{5}$$

where the mixture viscosity is defined as

$$\mu = \mu_l(1-\alpha_v)(1+2.5\alpha_v) + \mu_v\alpha_v, \quad \text{and} \tag{6}$$

μ_l and μ_v are the dynamic viscosity of water and vapor respectively. S_e and S_c are source terms for evaporation of water and condensation of vapor and are given by

$$\begin{aligned}S_e &= C_e\alpha_v^2(1-\alpha_v)^2\frac{\rho_l}{\rho_g}\frac{\max((p_v-p),0)}{\sqrt{2\pi R_g T}},\\ S_c &= C_c\alpha_v^2(1-\alpha_v)^2\frac{\max((p-p_v),0)}{\sqrt{2\pi R_g T}},\end{aligned} \tag{7}$$

where $p_v = 2.3$ kPa is the vapor pressure. $C_e(1/m)$ and $C_c(1/m)$ are the empirical constants based on the interfacial area as defined by Saito et al. (2007).

The isothermal mixture speed of sound is obtained by taking the derivative of the mixture equation of state (4) with respect to ρ at constant T. The expression for mixture sound speed is given in Appendix A. Note that the isothermal speed of sound is chosen to keep consistency with the isothermal assumption in the governing equations. The change in the speed of sound with gaseous phase volume fraction at a temperature of 298 K and a pressure of 0.1 MPa obtained from the computations is compared to the experimental data of Karplus (1957) in the Fig. 1. Note the good agreement with experiments in the mixture region. The effect of gas volume fraction in changing the acoustic characteristics of the water is evident by the orders of magnitude drop in the sound speed. The derivation of sound speed in the Eq. (A.1) does not account for the variation in Y_v, which implies no mass transfer between the phases. Hence, it is considered as the frozen speed of sound. Alternatively, if instantaneous mass transfer is assumed, then it is called the equilibrium speed of sound. Due to the finite rate of phase change, the speed of sound in a water-vapor mixture is lower than the frozen sound speed limit and higher than the equilibrium speed of sound limit (Franc and Michel, 2006). Sound speed in such cases depends on the accurate rate of phase change, subgrid-scale bubble dynamics, and non-condensable gas nuclei. Hence, it often depends on the problem. Analytical expressions for the speed of sound are available only in the limit of no mass transfer (i.e. frozen speed of sound) and equilibrium mass transfer (i.e. equilibrium speed of sound) (Franc and Michel, 2006). Bhatt and Mahesh (2020) showed very good agreement with the Ganesh et al. (2016) experiments for the bubbly shock propagation speed and vapor void fraction data using the frozen speed of sound. Hence, in this work, we retain the frozen speed of sound for our simulations. Note that the eigenvalues of the preconditioned convective Jacobian also yield the frozen speed of sound; and are therefore, consistent with the numerical modeling presented in Section 3.

3. Preconditioning with dual-time stepping

3.1. Vector form of the governing equations

The governing equations (Eq. (1)) are recast in the vector form as:

$$\frac{\partial U}{\partial t}+\frac{\partial F_j}{\partial x_j}=S, \quad \text{where}$$
$$U=\begin{pmatrix}\rho\\ \rho u\\ \rho v\\ \rho w\\ \rho Y_v\end{pmatrix}, \quad F_j=F_j^c+F_j^v,$$
$$F_j^c=\begin{pmatrix}\rho u_j\\ \rho u u_j+p\delta_{1j}\\ \rho v u_j+p\delta_{2j}\\ \rho w u_j+p\delta_{3j}\\ \rho u_j Y_v\end{pmatrix}, \quad F_j^v=\begin{pmatrix}0\\ \sigma_{1j}\\ \sigma_{2j}\\ \sigma_{3j}\\ 0\end{pmatrix}, \quad \text{and} \tag{8}$$
$$S=\begin{pmatrix}0\\ 0\\ 0\\ 0\\ S_e-S_c\end{pmatrix}.$$

Here, U is the vector of conserved variables, F is the flux vector, F^c is the convective part of the flux vector, F^v is the viscous part of the flux vector, and S is the source vector. δ_{ij} is the Kronecker delta function. For solving unsteady problems using preconditioning, a pseudo-time derivative term is added to the Eq. (8). Preconditioning is applied to the pseudo-time derivative to preserve the time accuracy of the unteady problem. The derivative term is written in terms of the time derivative matrix as:

$$\Gamma\frac{\partial Q}{\partial \tau}+\frac{\partial U}{\partial t}+\frac{\partial F_j}{\partial x_j}=S, \quad \text{where} \quad \Gamma=\frac{\partial U}{\partial Q},$$
$$Q=\begin{pmatrix}p\\ u\\ v\\ w\\ Y_v\end{pmatrix}, \quad \text{and} \quad \Gamma=\begin{pmatrix}\rho_p & 0 & 0 & 0 & \rho_{Y_v}\\ u\rho_p & \rho & 0 & 0 & u\rho_{Y_v}\\ v\rho_p & 0 & \rho & 0 & v\rho_{Y_v}\\ w\rho_p & 0 & 0 & \rho & w\rho_{Y_v}\\ Y_v\rho_p & 0 & 0 & 0 & Y_v\rho_{Y_v}+\rho\end{pmatrix}. \tag{9}$$

Here, Q is the primitive variable vector. Different choices of the primitive variables are possible (e.g. Kunz et al., 2000; Lindau et al., 2001; Venkateswaran et al., 2002). Lindau et al. (2001) and Venkateswaran et al. (2002) have shown that the choice of either α or Y_v as primitive variable leads to identical eigenvalues of the system. Here, we choose p and Y_v along with the velocity components as the primitive variables. Γ is the Jacobian matrix specifying the changes in the conserved variables with respect to the primitive variables. $\rho_p=\frac{\partial\rho}{\partial p}|_T$, which is inverse of the square of isothermal speed of sound ($\frac{1}{c^2}$). Similarly, $\rho_{Y_v}=\frac{\partial\rho}{\partial Y_v}|_T$. Expressions for these derivatives are given in Appendix A. The eigenvalues of the system of equation (Eq. (8)) can be obtained from the matrix $A_\Gamma=\Gamma^{-1}A$, where $A=\frac{\partial F}{\partial Q}$ is the convective flux Jacobian with respect to the primitive variable vector Q. The matrices A, Γ^{-1} and A_Γ are given in Appendix B. The eigenvalues of A_Γ are $\lambda_\Gamma=[V_n,V_n,V_n,V_n-c,V_n+c]$. Here, V_n is the velocity normal to the face. Note that in the low Mach regions, V_n is very small compared to c. Hence, the condition number of the matrix A_Γ is very high, which leads to the acoustic stiffness. This is a typical condition in the water with very low vapor nuclei.

3.2. Preconditioning

Time derivative preconditioning (Turkel, 1999) is used for the proper conditioning of A_Γ. ρ_p in the Γ matrix is modified as ρ_p' to construct the preconditioned time derivative matrix Γ_p as:

$$\Gamma_p=\begin{pmatrix}\rho_{p'} & 0 & 0 & 0 & \rho_{Y_v}\\ u\rho_{p'} & \rho & 0 & 0 & u\rho_{Y_v}\\ v\rho_{p'} & 0 & \rho & 0 & v\rho_{Y_v}\\ w\rho_{p'} & 0 & 0 & \rho & w\rho_{Y_v}\\ Y_v\rho_{p'} & 0 & 0 & 0 & Y_v\rho_{Y_v}+\rho\end{pmatrix}. \tag{10}$$

Note that the rest of the elements of the Γ_p matrix are the same as Γ. Here, $\rho_p'=\frac{1}{U_\infty^2}$ (Lindau et al., 2001). Note that for ρ_p' various other preconditioners can also be used (e.g. Venkateswaran et al., 2002; Ahuja et al., 2001). The eigenvalues of the preconditioned system can be obtained from the matrix $A_{p\Gamma}=\Gamma_p^{-1}A$. The matrices Γ_p^{-1} and $A_{p\Gamma}$ are given in Appendix B. The eigenvalues of $A_{p\Gamma}$ are $\lambda_{p\Gamma}=[V_n,V_n,V_n,\frac{1}{2}(V_n(1+\frac{c'^2}{c^2})-\sqrt{V_n^2(1-\frac{c'^2}{c^2})^2+4c'^2}),\frac{1}{2}(V_n(1+\frac{c'^2}{c^2})+\sqrt{V_n^2(1-\frac{c'^2}{c^2})^2+4c'^2})]$, where c' is the modified speed of sound based on $\rho_p'=\frac{1}{c'^2}$. Note that all the eigenvalues are of the order V_n; when $c'^2=1/\rho_p'=U_\infty^2$ is used for the preconditioning. Hence, the matrix $A_{p\Gamma}$ is well conditioned. Note that the pseudo-time derivative vanishes as one marches to the next time step in the physical-time. Hence, time accuracy is preserved when solving unsteady problems.

3.3. Time marching with DTS

The governing equation (Eq. (9)) after finite-volume integration and simplifications is given as,

$$\Gamma_p\frac{\partial Q}{\partial\tau}+\frac{\partial U}{\partial t}=R(U) \quad \text{where} \quad R(U)=-\frac{1}{\mathcal{V}}\int_{\mathcal{S}}F_j n_j d\mathcal{S}+\frac{1}{\mathcal{V}}\int_{\mathcal{V}}S d\mathcal{V}. \tag{11}$$

Here, $\mathcal{V}$ is the volume and S is the surface area of the cell. The time marching is performed using a *DTS* procedure (e.g. Vatsa and Turkel, 2003; Hsu and Jameson, 2002), where the physical-time derivative is discretized using a second order backward differencing (*BDF-2*) and the pseudo-time derivative is discretized using the explicit Euler. Alternatively, a fourth order Runge–Kutta (*RK-4*) method was considered for discretizing the pseudo-time derivative. However, overall cost of computing 4 stages of *RK-4* outweighed the CFL gain compared to the single step of the explicit Euler. Also, the explicit Euler is chosen for the simplicity of the preconditioned *DTS* framework. Indicating the current physical-time with 'n' and the pseudo-time with 'm', the discretized form of the equation is given as:

$$\Gamma_p\frac{Q^{m+1}-Q^m}{\Delta\tau}+\frac{3U^{n+1}-4U^n+U^{n-1}}{2\Delta t}=R(U^m). \tag{12}$$

Here, U^{n+1} is unknown. It is treated implicitly with respect to pseudo-time by considering it at $m+1$. Following the linearization $U^{m+1}=U^m+\Delta\tau\Gamma\frac{\Delta Q}{\Delta\tau}$, the Eq. (12) can be written as:

$$\left(\Gamma_p+\frac{3\Delta\tau}{2\Delta t}\Gamma\right)\frac{\Delta Q}{\Delta\tau}=R1(U^m), \quad \text{where}$$
$$R1(U^m)=-\left(\frac{3U^m-4U^n+U^{n-1}}{2\Delta t}\right)+R(U^m). \tag{13}$$

Here, $\Delta Q=Q^{m+1}-Q^m$. The matrices on the left-hand side can be combined as $\Gamma_{ip}=\Gamma_p+\frac{3\Delta\tau}{2\Delta t}\Gamma$. The pseudo-time marching is performed by inverting the matrix Γ_{ip}. Γ_{ip}^{-1} is given in the Appendix B. After the pseudo-time iterations are converged, the primitive variables are updated as $Q^{n+1}=Q^{m+1}$. Subsequently, the conserved variables are obtained from the primitive variables.

3.4. Shock capturing

Guillard and Viozat (1999) showed that preconditioning of the numerical dissipation term is necessary for the accurate scaling of the pressure fluctuations of the discrete system. They performed asymptotic analysis of the compressible Euler equation discretized using Roe's dissipation scheme, and proposed preconditioning of the numerical dissipation tensor to recover the correct scaling of the pressure. Turkel (1999) discusses various preconditioners for artificial dissipation terms. Turkel (1999) shows that different choices for variables and preconditioners can be used in the time derivative matrix and the artificial dissipation term. Also, it is suggested that if one wishes to capture shocks, the fluxes be evaluated in terms of conserved variables (U) and subsequently preconditioned. Hence, for shock capturing the conservative variables are retained.

The convective fluxes can be written as the sum of the central part and the dissipation part as:

$$F^c = F^c_c + F^c_d. \tag{14}$$

Here, F^c_c is the central part, which is discretized using a symmetric non-dissipative finite volume scheme, where fluxes at a cell face are given by

$$\phi_{f_c} = \frac{\phi_{icv1} + \phi_{icv2}}{2} + \frac{1}{2}(\nabla\phi|_{icv1} \cdot \Delta\mathbf{x}^{icv1} + \nabla\phi|_{icv2} \cdot \Delta\mathbf{x}^{icv2}), \tag{15}$$

where $\Delta\mathbf{x}^{icv1} = \mathbf{x}_{f_c} - \mathbf{x}_{icv1}$, and $\nabla\phi|_{icv1}$ denotes gradient defined at $icv1$, which is computed using a least-squares method. '$icv1$' is the current cell, '$icv2$' is the neighbouring cell, and 'fc' is the common face. The viscous fluxes are split into the compressible and the incompressible contributions, and treated separately. See (Gnanaskandan and Mahesh, 2015) for the details.

F^c_d is the dissipation part, which is treated using the characteristic based filtering (Yee et al., 1999). Originally, the method was developed by Yee et al. (1999) for ideal gases on structured grids. Park and Mahesh (2007) extended this to unstructured grids. Gnanaskandan and Mahesh (2015) extended this to the mixture of fluids and the mixture equation of state used in the present work. They implemented the methodology in a predictor-corrector manner, where the filtering is applied in the corrector step. Alternatively, the filtering can also be directly applied for the dissipative part of the flux in a single step as discussed in Yee et al. (1999). In the present work, we compute both the central part and the dissipation part in a single step as shown in the Eq. (14). It is done for the simplicity in adopting the fluxes in a *DTS* framework. The formulation for the characteristic filtering is the same as used in Gnanaskandan and Mahesh (2015). However, the eigenvalues are modified to obtain the proper conditioning at the low Mach numbers. F^c_d in the characteristic filtering is of the following form:

$$F^c_{df_c} = \frac{1}{2} R_{f_c} \Phi_{fc}. \tag{16}$$

Here, R_{f_c} is the matrix of right eigenvectors of the Jacobian $B = \frac{\partial F}{\partial U}$. It is computed at the face using the Roe average of the variables from the left and the right cell-centered values. The matrices R, R^{-1} and B are given in the Appendix of Gnanaskandan (2015). Φ^*_{fc} is a vector, lth component of which, ϕ^{*l}, is given by

$$\phi^{*l}_{fc} = k\theta^l_{fc}\phi^l_{fc}, \tag{17}$$

where k is an adjustable parameter and θ_{fc} is Harten's switch function, given by

$$\theta_{fc} = \sqrt{0.5(\hat{\theta^2_{icv1}} + \hat{\theta^2_{icv2}})}, \quad \hat{\theta_{icv1}} = \frac{|\beta_{fc}| - |\beta_{f1}|}{|\beta_{fc}| + |\beta_{f1}|},$$
$$\hat{\theta_{icv2}} = \frac{|\beta_{f2}| - |\beta_{fc}|}{|\beta_{f2}| + |\beta_{fc}|}. \tag{18}$$

Here, $\beta_f = R_f^{-1}(U_{icv2} - U_{icv1})$ is the difference between characteristic variables across the face. q For ϕ_l, the Harten–Yee total variation diminishing (TVD) form is used as suggested by Yee et al. (1999):

$$\phi^l_{fc} = \frac{1}{2}\Psi(a^l_{fc})(g^l_{icv1} + g^l_{icv2}) - \Psi(a^l_{fc} + \gamma^l_{fc})\beta^l_{fc},$$
$$\gamma^l_{fc} = \frac{1}{2}\frac{\Psi(a^l_{fc})(g^l_{icv2} - g^l_{icv1})\beta^l_{fc}}{(\beta^l_{fc})^2 + \epsilon}, \tag{19}$$

where $\epsilon = 10^{-7}$, $\Psi(z) = \sqrt{\delta + z^2}$ (δ being 1/16) is introduced for entropy fixing and a^l_{fc} is an eigenvalue of the Jacobian matrix B.

B has the set of eigenvalues $\lambda_B = [V_n, V_n, V_n, V_n - c, V_n + c]$. Note that the matrix is ill-conditioned in the low Mach limit. One way to rectify this is to use a typical low-speed preconditioner (e.g. Weiss and Smith, 1995). This works well in the incompressible limit. However, for cavitating flows Mach numbers can range from the extremely low values in the water to the supersonic regions in the mixture. Hence, in the present work, we use an all-Mach preconditioning approach proposed by Li and Gu (2008). The implementation of this approach is straight-forward as it only involves changes in the eigenvalues of B, keeping both the Jacobian matrix and the eigenvector matrix the same. Li and Gu (2008) discusses this in detail. Following that, we modify the eigenvalues as:

$$\lambda_B = [V_n, V_n, V_n, V_n - f(M)c, V_n + f(M)c], \quad \text{where}$$
$$f(M) = min(M^2, 1). \tag{20}$$

Here, $f(M)$ is a function of local Mach number that satisfies the following three criteria:

$$0 < f(M) < 1 \quad \text{when} \quad 0 < M < 1$$
$$f(M) \to 0 \quad \text{when} \quad M \to 0$$
$$f(M) = 0 \quad \text{when} \quad M >= 1$$

The limiter function g_{icv} is computed using the minmod limiter. Park and Mahesh (2007) and Gnanaskandan and Mahesh (2015) proposed a modification to the Harten switch to accurately represent under-resolved turbulence for single phase and multi phase flow mixtures respectively by multiplying θ_{f_c} with $\theta^\star_{f_c}$ given by

$$\theta^\star_{f_c} = \frac{1}{2}\left(\theta^\star_{icv1} + \theta^\star_{icv2}\right) + |(\alpha_{icv2} - \alpha_{icv1})|, \tag{21}$$
$$\theta^\star_{icv1} = \frac{(\nabla \cdot \mathbf{u})^2_{icv1}}{(\nabla \cdot \mathbf{u})^2_{icv1} + \Omega^2_{icv1} + \epsilon}.$$

3.5. Rotating frame of reference

For simulating flow over a propeller in Section 4.3, we use rotating frame of reference approach. The governing Eqs. 1 are filtered for LES and the sub-grid terms are modeled using the Dynamic Smagorinsky Model (DSM) (Moin et al., 1991). For rotating frame of reference we use absolute velocity formulation as discussed in Bhatt and Mahesh (2019). The governing Eq. (1) after LES filtering can be written in rotating frame of reference in terms of absolute velocity as:

$$\frac{\partial \overline{\rho}\tilde{u}_i}{\partial t} = -\frac{\partial}{\partial x_k}(\overline{\rho}\tilde{u}_i\tilde{u}_k + \overline{p}\delta_{ik} - \tilde{\sigma}_{ik} - \tau_{ik}) + \frac{\partial}{\partial x_k}\left(\overline{\rho}\tilde{u}_i\epsilon_{kjl}w_j x_l\right) + \rho\epsilon_{ijk}w_j u_{r_k}. \tag{22}$$

Here, w is angular velocity of rotating frame of reference. Absolute velocity u is related to the velocity in rotating reference frame (u_r) as $u = u_r + \epsilon_{ijk}w_j x_k$. Eq. (22) is solved in rotating frame of reference in terms of absolute velocity, therefore it does not invole any contribution due to centrifugal force. This also simplifies the

Table 1
Details of the simulations conducted for the flow over a cylinder at $Re = 200$. Here, α_{ν_∞} is the free-stream nuclei content, and M_∞ is the free-stream Mach number.

Cases simulated	(α_{ν_∞})	M_∞	Description
Case-O	10^{-2}	0.01	Original solver - no preconditioning (Gnanaskandan and Mahesh, 2015)
Case-OLM	10^{-6}	0.001	Original solver at low Mach
Case-P	10^{-2}	0.01	Preconditioning with *DTS*
Case-PLM	10^{-6}	0.001	Preconditioning with *DTS* at low Mach
Case-PRLM	10^{-6}	0.001	Preconditioning with *DTS* with *RS* at low Mach

boundary condition implementation as it is now applied to absolute velocity directly. Note that this formulation adds additional contribution due to the Coriolis force and modifies the advection terms in the governing Eq. (1). Changes in the advection terms subsequently requires modification to the shock capturing of the method. This additional contribution due to rotation indeed only changes the diagonal of the jacobian matrix. Thus the preconditioned eigenvalues in Eq. (20) can be modified as:

$$\lambda_B = [V_n^{'}, V_n^{'}, V_n^{'}, V_n^{'} - f(M)c, V_n^{'} + f(M)c]. \tag{23}$$

Here, $V_n^{'} = V_n - (w \times r).\hat{n}$, where r is the radial vector from axis of rotation and $\hat{n}$ is the unit normal vector.

4. Results

We assess the methodology using the following numerical experiments. First, we consider the unsteady flow over a cylinder under wetted conditions. The problem is used to assess the preconditioning and *DTS* framework for the unsteady low Mach number problem in water. Various aspects of the simulation such as total run-time, shedding frequency, pressure, and velocity field are considered for comparison and analysis. Next, the background pressure is dropped to examine cavitation inception in the cylinder configuration. Here, the method is assessed for its ability to handle the small scale vapor regions at the low free-stream nuclei concentration. Finally, the ability of the method to extend to the complex problems is assessed by doing the LES of flow over a marine propeller under wetted conditions. The calculations were previously very expensive and formidable due to the convergence issues at low Mach numbers. In the simulations, we discuss run-time, the effect of free-stream nuclei on the propeller loads, and comparison to both the experiments and the incompressible solver results.

4.1. Unsteady flow over a cylinder

We simulate the flow over a circular cylinder at Reynolds number $(\mathrm{Re}) = \frac{\rho_\infty U_\infty D}{\mu_\infty} = 200$, where the subscript '$\infty$' represents the free-stream values and D is the cylinder diameter. The domain size and mesh used in the present study are the same as those considered in Brandao et al. (2020) and Gnanaskandan and Mahesh (2016b). Gnanaskandan and Mahesh (2016b) performed a grid refinement study and showed that the time evolution of the drag coefficient and the profiles of the mean and the fluctuations in the void fraction show a good agreement among the chosen grids. To avoid the reflection of pressure waves from the boundaries, a large domain of $50D$ is used. Also, we apply acoustically absorbing sponge layers at the boundaries (Colonius, 2004) to further reduce any reflections. The simulations are initialized with a spatially uniform void fraction of vapor (α_{ν_∞}) as a background nuclei. The flow Mach number is changed by choosing different values of free-stream nuclei. Table 1 summarizes the simulated cases. All the cases are simulated at a cavitation number $(\sigma) = \frac{p - p_v}{0.5\rho_\infty U_\infty^2} = 5$, such that no cavitation is observed. Only the free-stream nuclei are varied that change the free-stream Mach number, and consequently the acoustic stiffness. The changes in Mach number are within the incompressible limit, thus, the unsteady vortex shedding is expected to be identical for the considered cases.

Fig. 2 shows the instantaneous snapshots of $\tilde{u}$ and $\tilde{p}$ for 3 cases: (i) original solver of Gnanaskandan and Mahesh (2015) at high Mach number (Case-O), (ii) original solver at low Mach number (Case-OLM) and (iii) preconditioning with dual time stepping at low Mach number (Case-PLM); respectively in the Fig. 2(a)–(c). Here, $\tilde{u} = u/U_\infty$ is the non-dimensional axial component of the velocity, and $\tilde{p} = \frac{p}{\rho_\infty U_\infty^2}$ is the non-dimensional pressure. For the Case-O, the sinusoidal velocity field and the pockets of low-pressure cores of the vortices indicate that the compressible solver is reasonably capturing the vortex shedding at this Mach number. However, at low Mach numbers, for Case-OLM, the pressure field is completely intangible. This is due to the incorrect scaling of the pressure field for the compressible solver in the incompressible limit (Turkel, 1999). Interestingly, the Case-PLM shows that with the use of preconditioning, the accurate pressure field is retained even at low Mach number (Case-PLM).

We consider Case-O as the baseline to compare the Case-PLM. The profiles of the mean pressure and the root-mean-squared (*RMS*) pressure are chosen for the comparison and shown in the Figs. 3 and 4 respectively. Very good agreement is observed in both the mean pressure and the *RMS* pressure with the Case-O. This demonstrates the ability of the methodology with preconditioning to capture the accurate pressure field at low Mach numbers.

The Strouhal number for the vortex shedding is obtained as $St = \frac{fD}{U_\infty}$. Here, 'f' is the vortex shedding frequency obtained from the Fast Fourier Transform (*FFT*) of the time-history of the drag coefficient. It is compared to the canonical study of Williamson (1996) in the Table 2. Note good agreement with the (Williamson, 1996) for both the Case-O and Case-PLM. Interestingly, the Case-PLM shows a better comparison to Williamson (1996) than Case-O. The identical values the St for both Case-P and Case-PLM indicates that the St is not affected by the flow Mach number when the preconditioning is used.

In addition to improving the solution accuracy, preconditioning significantly reduces computer time. The Table 3 compares the computer time for all the cases simulated. At low Mach number, the time step for the compressible solver drops by a factor of 50 from 5×10^{-5} to 1×10^{-6}. This increases the total run-time from 33.5 min to 1 day for 1 cycle of vortex shedding. Therefore, we can see that the acoustic stiffness due to disparities in eigenvalues at low Mach numbers significantly affects the run-time. The acoustic stiffness is eliminated with the use of preconditioning as observed in Table 3 for Case-P, Case-PLM, and Case-PRLM. A significantly higher physical-time step of 1×10^{-2} can be used with the preconditioning. Also, the physical-time step is independent of the Mach number. The calculations can be further accelerated by using the residual smoothing (*RS*) (e.g. Vatsa and Turkel, 2003) for the convergence of the pseudo-time step. The *RS* increases pseudo-time step by a factor of 3 from 2×10^{-3} to 6×10^{-3} and reduces the total run-time by half.

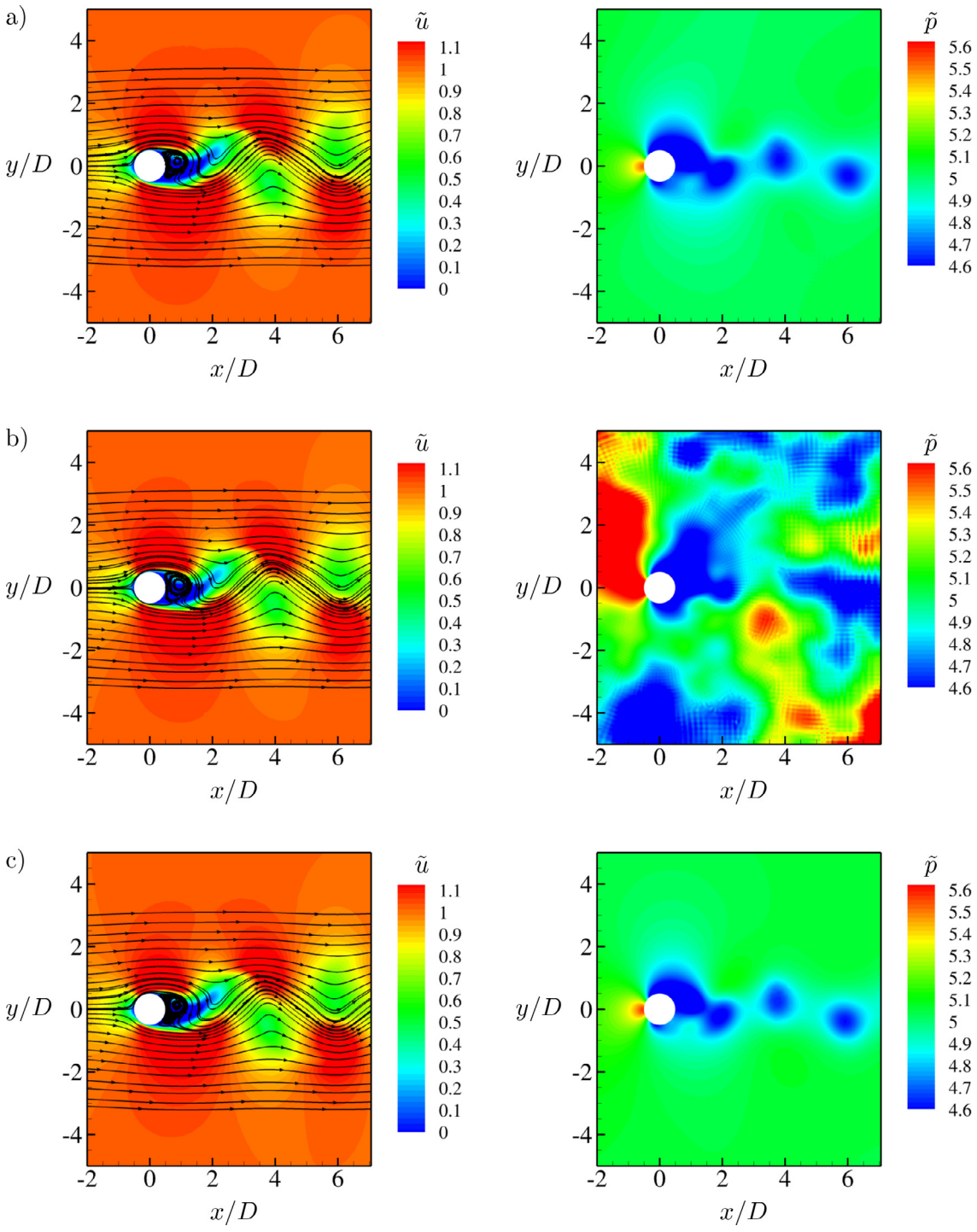

Fig. 2. Unsteady flow over a cylinder at $Re = 200$. (a) Case-O, (b) Case-OLM, and (c) Case-PLM. Instantaneous snapshots of $\tilde{u}$ (on the left), and $\tilde{p}$ (on the right).

Table 2
Comparison of the St for the flow over a cylinder at $Re = 200$. St is computed from the frequency obtained from the Fast Fourier Transform (FFT) of the time-history of the drag coefficient.

	Case-O	Case-OLM	Case-P	Case-PLM	(Williamson, 1996)
$St = fD/U_\infty$	0.198	×	0.184	0.184	0.182

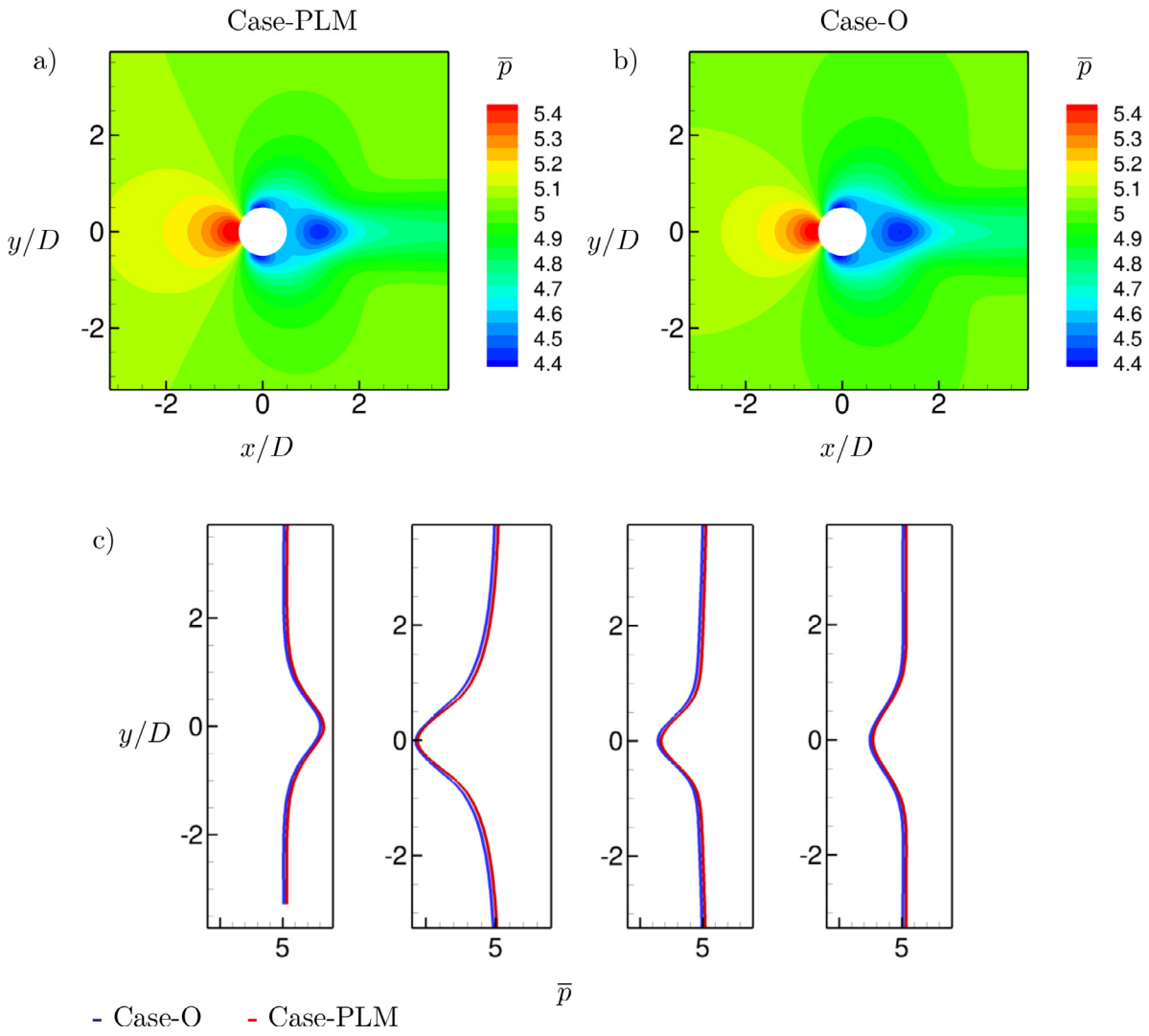

Fig. 3. Comparison of the mean pressure profiles ($\overline{p}$) for the unsteady flow over a cylinder at $Re = 200$. (a) Contours of $\overline{p}$ for Case-PLM, and (b) Case-O. (c) Profiles extracted along the y-axis at $x/D = -1.0$, 1.0, 2.0 and 3.0.

Table 3
Computational time for the cases simulated for the flow over a cylinder at $Re = 200$. Here, Δt is the physical-time step, $\Delta\tau$ is the pseudo-time step, and n_{itr} is the number of pseudo-time iterations per physical-time step.

Cases simulated	Δt	$\Delta\tau$	run-time/cycle	n_{itr}
Case-O	5×10^{-5}	–	33.5 min	–
Case-OLM	1×10^{-6}	–	1 day	–
Case-P	1×10^{-2}	2×10^{-3}	6.18 min	30
Case-PLM	1×10^{-2}	2×10^{-3}	5.6 min	30
Case-PRLM	1×10^{-2}	6×10^{-3}	3.7 min	11

4.2. Cavitation inception over a cylinder

In this section, we consider the flow at $\sigma = 1.8$. The only difference from the calculations presented in Section 4.1 is that the free-stream pressure is dropped to allow cavitation; thereby, changing σ from 5 to 1.8. For σ lower than 1.8, Brandao et al. (2020) discuss the developed cavitation regimes in detail. They show that at $\sigma = 1$, the cavitation is observed in the vortex core as the local pressure inside the core drops below vapor pressure; this is termed as the cyclic regime. If σ is further reduced to 0.7, the pressure in the near wake of the cylinder also drops below vapor pressure. This leads to transitional shedding by condensation shock propagation. Given this prior work, the current development allows us to extend to higher σ close to cavitation inception, with the significant time savings. The details of the flow conditions are given in Table 4 and the corresponding computer time requirements are given in Table 5. Note that changing the cavitation number does not affect the time step and the overall run-time when preconditioning is used (compare the case in Table 5 to the cases in Table 3). A significant saving in the run-time over the original solver (compare Case-OLM with Case-I) is obtained at low Mach number.

The solution is visualized using the instantaneous snapshots of Y_v and $\tilde{p}$. Three snapshots are chosen to cover a single vortex shedding cycle from the bottom of the cylinder. $\tilde{p}$ is plotted on a log scale from 0.01 to 1. The corresponding non-dimensional value of the vapor pressure is 0.011. Hence, the blue regions observed at the bottom of the cylinder surface in the Fig. 5(a) indicate the local pressure lower than the vapor pressure. Unlike in the cyclic cavitation regime discussed by Brandao et al. (2020) at $\sigma = 1$; here at $\sigma = 1.8$, the regions within the vortex core yield

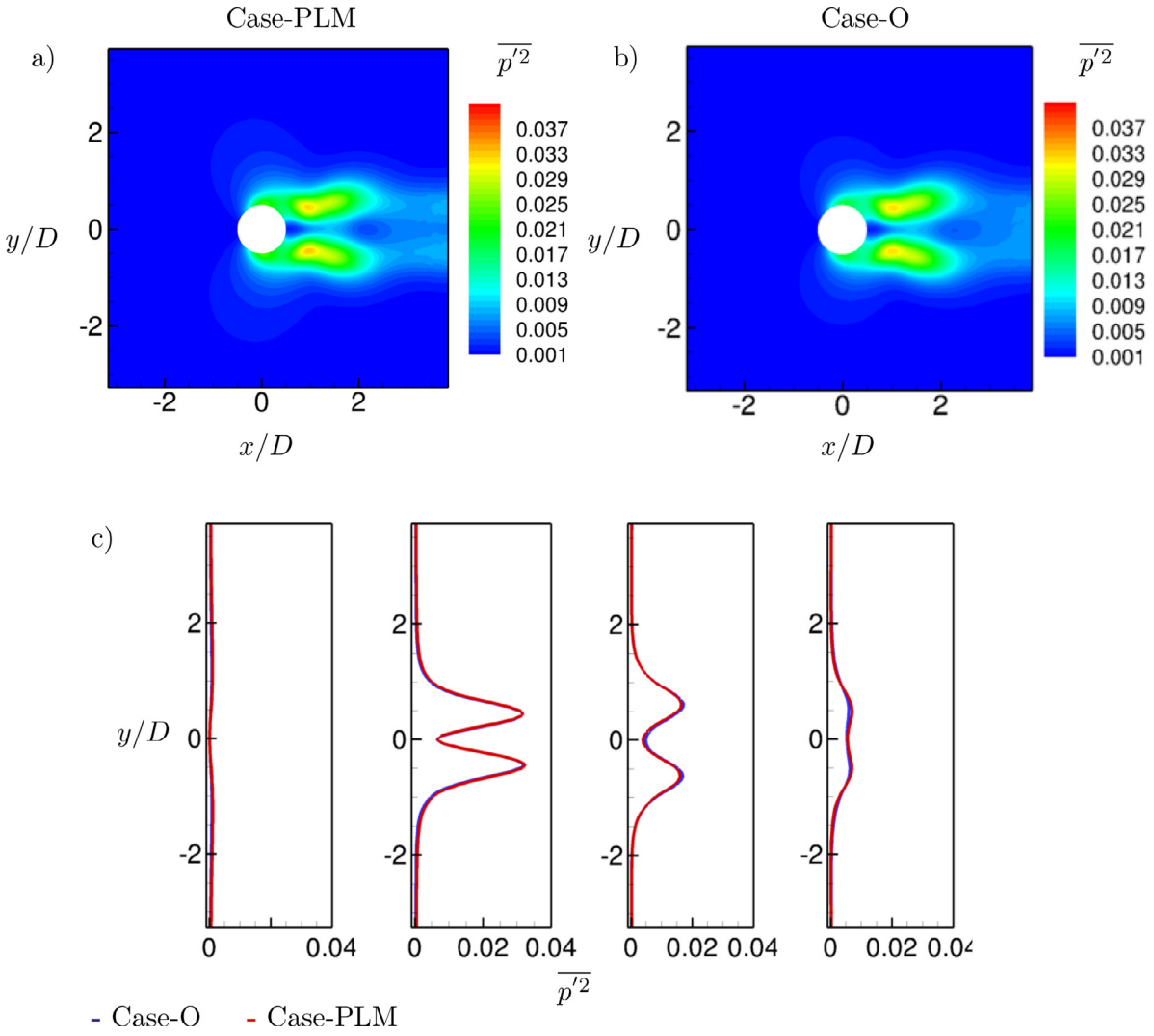

Fig. 4. Comparison of the *RMS* pressure profiles ($\overline{p'^2}$) for the unsteady flow over a cylinder at $Re = 200$. (a) Contours of $\overline{p'^2}$ for Case-PLM, and (b) Case-O. (c) Profiles extracted along the y-axis at $x/D = -1.0$, 1.0, 2.0 and 3.0.

Table 4
Details of the simulations conducted for the cavitation inception over a cylinder. Here, α_{ν_∞} is the free-stream nuclei content, and M_∞ is the free-stream Mach number.

Case simulated	(α_{ν_∞})	M_∞	Re	σ	Description
Case-I	10^{-6}	0.001	200	1.8	Preconditioning with *DTS* with *RS* at low Mach

Table 5
Computational time for the simulation of the cavitation inception over a cylinder. Here, Δt is the physical-time step, and $\Delta\tau$ is the pseudo-time step.

Cases simulated	Δt	$\Delta\tau$	run-time/cycle
Case-I	1×10^{-2}	2×10^{-3}	4.17 min

local pressure higher than the vapor pressure. This suggests that the vapor is incepted on the cylinder surface and advected downstream along the shear-layer into the vortex core. In the subsequent snapshots, after the vortex is shed from the bottom, the low pressure now appears on the top of the cylinder (Fig. 5) continuing the periodic shedding. The St remains unchanged from the non-cavitation conditions as shown in Table 2. Overall, the Y_ν remains of the $O(10^{-7})$, which is 3 orders of magnitude lower

Table 6
Details of the simulations conducted for the LES of high Re flow over a propeller under wetted conditions. Here, α_{ν_∞} is the free-stream nuclei content, and M_∞ is the free-stream Mach number.

Cases simulated	(α_{ν_∞})	M_∞	Description
Case-O	10^{-2}	0.03	Original solver - no preconditioning (Gnanaskandan and Mahesh, 2015)
Case-OLM	10^{-4}	0.005	Original solver at low Mach
Case-PRLM	10^{-6}	0.002	Preconditioning with *DTS* with *RS* at low Mach

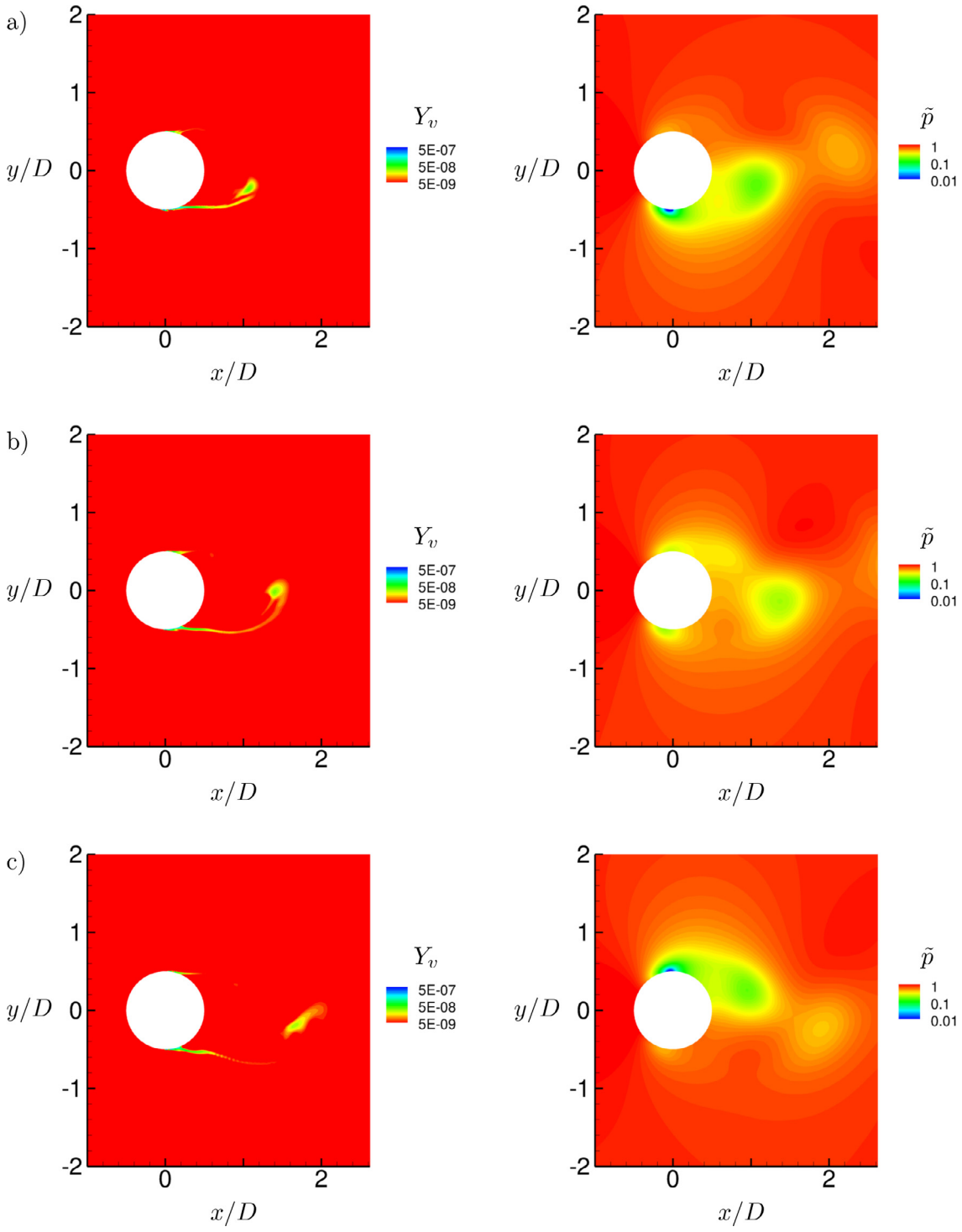

Fig. 5. Cavitation inception on the cylinder at $Re = 200$ and $\sigma = 1.8$. (a) Beginning of the vortex shedding, (b) $t = 0.42$ cycle and (c) $t = 0.84$ cycle. Instantaneous snapshots of Y_v (on the left), and $\tilde{p}$ (on the right).

than what was observed in the developed cavitation regimes (Brandao et al., 2020).

4.3. LES of flow over a propeller under wetted conditions

We simulate flow over a five-bladed marine propeller P4381 at the design advance ratio, $J = 0.89$, $Re = 894,000$, and $\sigma = \infty$ (i.e. under wetted conditions). The advance ratio is defined as $J = \frac{U_\infty}{nD}$, where n is the rotation rate and D is the propeller diameter. Bhatt and Mahesh, (2019) simulated the flow with the above conditions using the original solver of Gnanaskandan and Mahesh (2015). They found that the propeller loads are very sensitive to the free-stream nuclei concentration. Also, they obtained closer comparison to the experiments when the free-stream nuclei concentration was reduced from 0.01 (i.e. a typical high nuclei concentration prescribed in the numerical solver to avoid acoustic stiffness (e.g. Saito et al., 2007)) to 0.0001. However, a further reduction in the nuclei concentration could not be achieved as it sig-

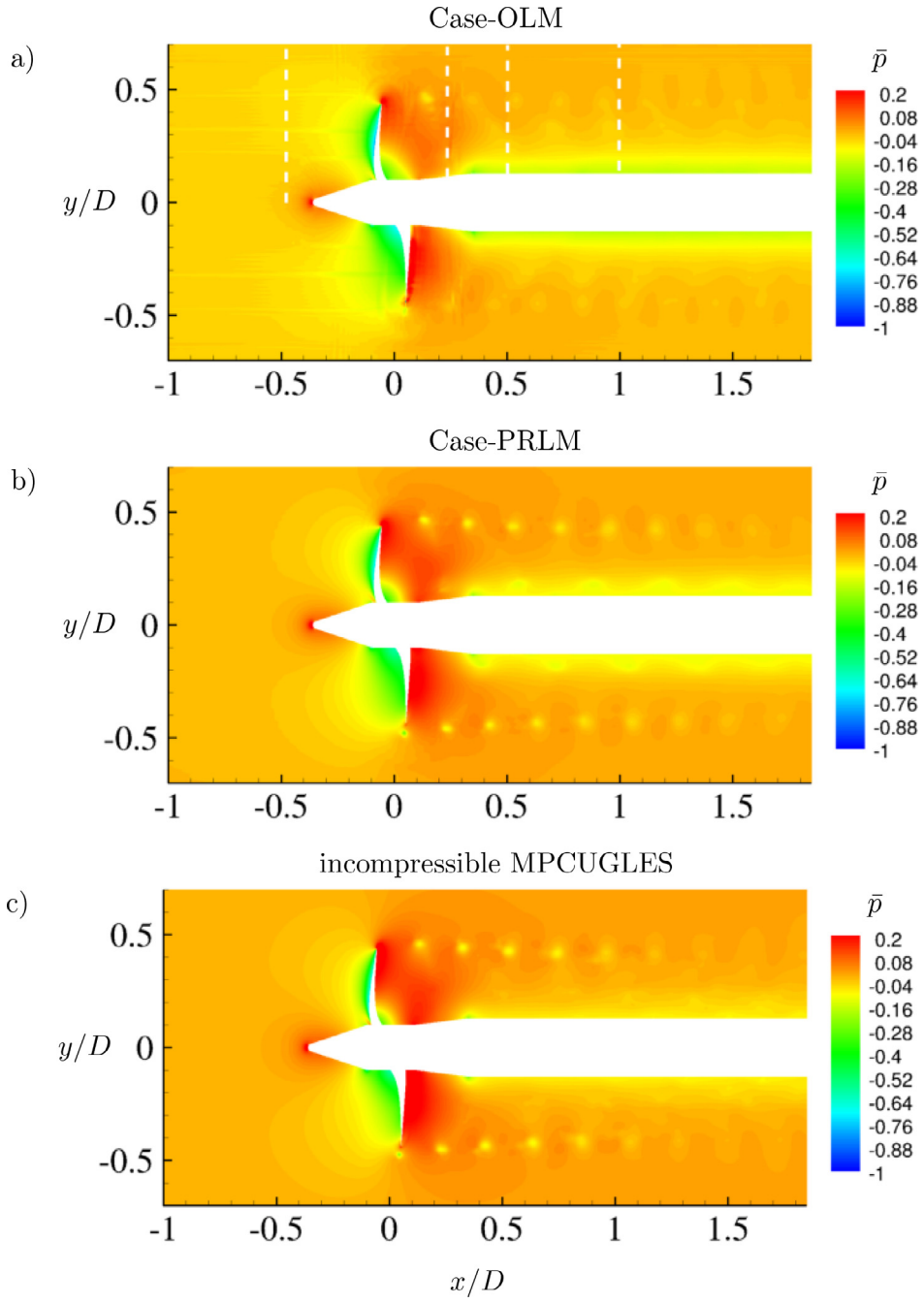

Fig. 6. Contours of the phase averaged pressure field along the $x-y$ plane for $Re = 894,000$ flow over the P4381 propeller under the wetted conditions. (a) Case-OLM, (b) Case-PLM and (c) incompressible MPCUGLES (Mahesh et al., 2004). The flow is from left to right.

nificantly reduced the time step and increased the total run-time. Here, with the preconditioning and *DTS*, we show that the calculations can be performed at such low free-stream nuclei in a reasonable amount of time. Table 6 summariez the cases considered in Bhatt and Mahesh (2019) along with the current simulations.

The computational domain/grid and boundary conditions are kept the same as considered in Bhatt and Mahesh (2019) and the preconditioning method is applied here. Bhatt and Mahesh (2019) assessed the grid refinement and numerical dissipation from the shock-capturing for this problem. Here, we consider the grid consisted of 11,532,735 hexahedral control volumes. We apply an acoustically absorbing sponge layer spanning a distance of D at the inflow, outflow and, the far-field boundaries to avoid reflections of pressure waves. We apply pressure Neumann boundary conditions at the outflow.

First, we compare the propeller loads obtained from the current simulations to Bhatt and Mahesh (2019) and the experimental data of Boswell (1971) in the Table 7. The notation used for propeller performance is as follows. The thrust (T) is the axial component of a force and the torque (Q) is the axial component of the moment of force. Non-dimensional thrust coefficient is defined as $K_T = \frac{T}{\rho n^2 D^4}$ and the torque coefficient is defined as $K_Q = \frac{Q}{\rho n^2 D^5}$. Forces are averaged over 4 propeller revolutions. Bhatt and Mahesh (2019) showed that a better comparison to the experiments can be obtained at lower values of free-stream nuclei. This is evident from comparing K_T and K_Q for Case-O and Case-OLM to

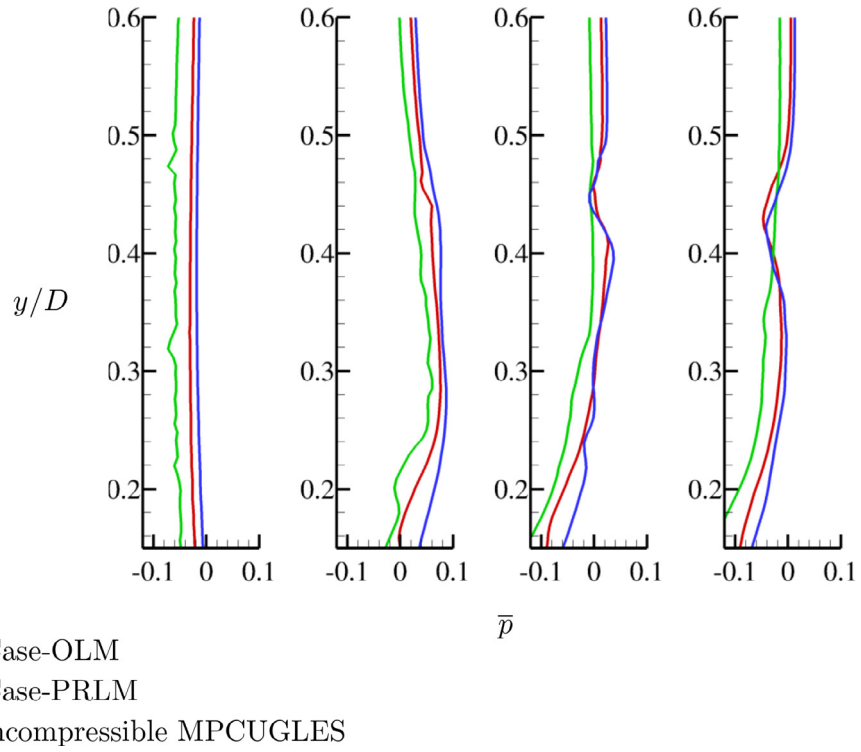

Fig. 7. Profiles of the phase averaged pressure field for the $Re = 894,000$ flow over the propeller P4381 under the wetted conditions. The profiles are extracted along the y-axis at $x = -0.5D$, $0.25D$, $0.5D$ and $1.0D$.

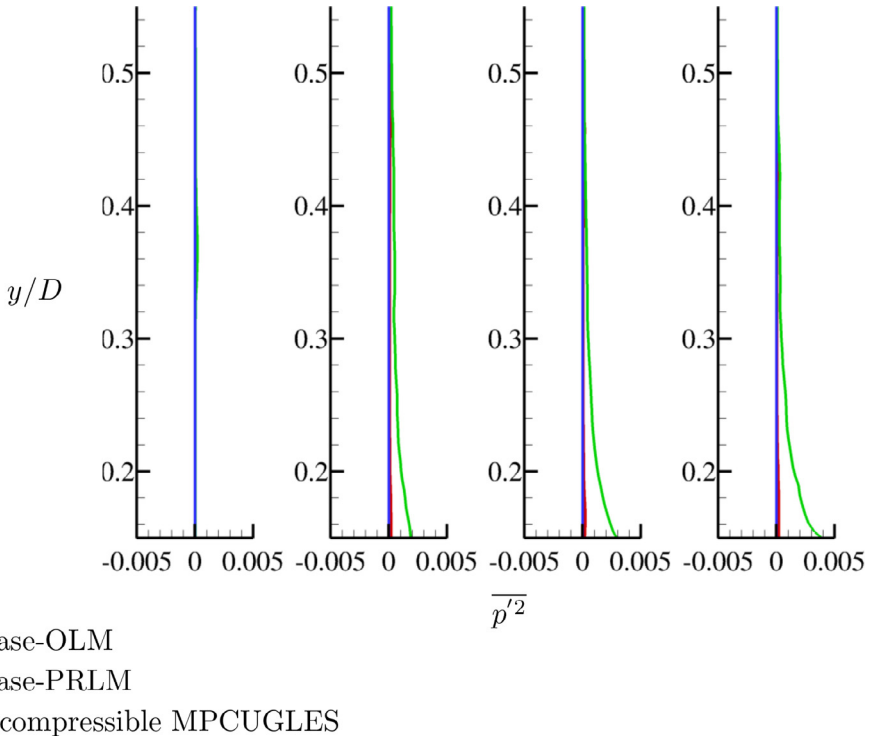

Fig. 8. Profiles of the *RMS* pressure fluctuations for the $Re = 894,000$ flow over the propeller P4381 under the wetted conditions. The profiles are extracted along the y-axis at $x = -0.5D$, $0.25D$, $0.5D$ and $1.0D$.

Boswell (1971) experiments. Case-OLM shows a better comparison to the experiments. The preconditioning allowed the calculations at an even lower nuclei concentration (Case-PRLM) (consequently, at a very low Mach). The preconditioning case shows a significant improvement in the K_Q from the prior study. Overall, both the K_T and K_Q of the Case-PRLM show a very good comparison to the experiments.

As discussed in Section 4.1, for low Mach number flows it is important to assess the pressure field obtained from the compressible solver. Hence, we compare the mean and the *RMS* pressure field

Table 7
Comparison of propeller performance under the wetted conditions.

	K_T	K_Q
Case-O	0.257	0.055
Case-OLM	0.226	0.050
Case-PRLM	0.227	0.0458
(Boswell, 1971)	0.215	0.045

Table 8
Computational time for the cases simulated for the at $Re = 894,000$ flow over the propeller p4381 under the wetted conditions. Here, Δt is the physical-time step, and $\Delta\tau$ is the pseudo-time step.

Cases simulated	Δt	$\Delta\tau$	run-time/cycle
Case-OLM	2×10^{-6}	–	~ 2 weeks
Case-PRLM	5×10^{-3}	1×10^{-3}	~ 40 h

of the original solver (Case-OLM) and the preconditioned solver (Case-PRLM) with the incompressible MPCUGLES (Mahesh et al., 2004). The incompressible solver is considered as the baseline since the M_∞ is less than 0.01. The contours of the mean pressure field are visualized in Fig. 6. For the Case-OLM the horizontal stripes upstream of the propeller, the lack of visibility of the tip vortices, and the diffused regions of low pressure close to the shaft are all indicators of the deteriorated pressure field. This behavior is similar to what was observed for the cylinder case in Section 4.1. As noted earlier, it is due to the incorrect scaling of the pressure field for the compressible solver in the incompressible limit (Turkel, 1999). With the use of preconditioning (Case-PRLM), the improvement on all the fronts is observed. This is evident visually from the comparison of the Case-PRLM to the incompressible MPCUGLES. The secondary vortices close to the shaft of the propeller are better captured in the Case-PRLM. A quantitative comparison of the mean pressure is obtained by taking profiles along the y-axis at various axial locations as indicated by the white dashed lines in Fig. 6(a). The profiles are compared in Fig. 7. For Case-OLM, even the mean pressure upstream of the propeller at $x = -0.5D$ is different from the baseline incompressible MPCUGLES. Also, the profile shows oscillations along the y-axis. Both Case-PRLM and incompressible MPCUGLES are generally in good agreement at all the locations. The lower pressures near the shaft at $x = 0.25D$ and $x = 0.5D$ for the Case-PRLM are due to the secondary vortices near the shaft as visualized in the Fig. 6(b). The *RMS* pressure is compared in the Fig. 8. The pressure fluctuations are typically very small for the low Mach number flow. However, the Case-OLM shows very high-pressure fluctuations close to the shaft; particularly at the locations downstream of the propeller blade (i.e. $x = 0.25D$, $x = 0.5D$ and $x = D$). Here also, the Case-PRLM is generally in good agreement with the incompressible solution.

Finally, we compare the computational time savings when using preconditioning as compared to the original solver in the Table 8. The preconditioning allows a significantly higher physical-time step of 5×10^{-3} as compared to the physical-time step of 2×10^{-6} of the original solver. Although, the overall gain in the run-time is not directly proportional to the time step gain as the additional time is needed to converge the pseudo-time derivative at each physical-time step. Nevertheless, preconditioning saves the run-time significantly from ~ 2 weeks to ~ 40 h per cycle.

5. Summary

A numerical approach based on preconditioning and *DTS* is applied to a fully compressible (density-based) cavitating solver (Gnanaskandan and Mahesh, 2015). The methodology is based on the homogeneous mixture model and finite rate mass transfer. The time-derivative preconditioning matrix is constructed using the mass fraction formulation for the primitive variables. The speed of sound is preconditioned based on the free-stream velocity as discussed by Lindau et al. (2001). The preconditioned system of equation is shown to be well-conditioned from the resulting eigenvalues of the flux-Jacobian matrix. The shock-capturing based on the characteristic-based filtering is modified by following the all-speed approach suggested by Li and Gu (2008) for Roe-type schemes. Also, the conserved variables are retained for preconditioning the shock-capturing to ensure conservation across shocks and contact discontinuities.

The method is demonstrated for cavitation inception and wetted flow conditions over a cylinder at $Re = 200$. The limitation of the original solver for capturing the pressure field at low Mach number is shown using the instantaneous solution. The flow-field is compared to the high Mach number solution as a baseline and the shedding frequency is validated with (Williamson, 1996). The preconditioning allowed accurate computation of both the mean pressure and pressure fluctuations at low values of free-stream nuclei. Overall, a significant saving in the total run-time from ~ 1 day/cycle to ~ 4 min/cycle is obtained using the preconditioning compared to the original solver. Given the prior work of Brandao et al. (2020) on the developed cavitation over the cylinder, the current development allowed the extension to the cavitation inception regime. The methodology is demonstrated for flow over a marine propeller under wetted conditions at $Re = 894,000$ using the LES. The preconditioning methodology allowed the low free-stream nuclei calculations in a reasonable amount of run-time that were formidable in the earlier study of Bhatt and Mahesh (2019). A very good comparisons for the thrust and torque with the (Boswell, 1971) experiments is obtained. Also, good comparions of the mean pressure and pressure fluctuations with the incompressible solver (Mahesh et al., 2004) are obtained.

Declaration of Competing Interest

The authors declare that they have no known competing financial interests or personal relationships that could have appeared to influence the work reported in this paper.

Acknowledgments

This work is supported by the United States Office of Naval Research under grant ONR N00014-17-1-2676 with Dr. Ki-Han Kim as the program manager. The computations were made possible through the computing resources provided by the High-Performance Computing Modernization Program (HPCMP), Texas Advance Computing Center (TACC), and the Minnesota Supercomputing Institute (MSI).

Appendix A. Derivatives

The expressions for the derivatives appearing in the time derivative matrix (Eq. (9)) are derived by substituting the equation of state (Eq. (4)) in terms of density, and then taking its derivative at constant T. They are given as:

$$\begin{aligned}\rho_{Y_v} &= \frac{\partial \rho}{\partial Y_v}\bigg|_T \\ &= \rho^2\left(\frac{1}{\rho_l} - \frac{1}{\rho_v}\right), \quad \text{and} \\ \rho_p &= \frac{\partial \rho}{\partial p}|_T = \frac{1}{c^2} \\ &= \frac{2p + P_c - \rho Y_v RgT - (1 - Y_v)\rho K_l T}{(p + P_c)Y_v RgT + p(1 - Y_v)K_l T}.\end{aligned} \tag{A.1}$$

Appendix B. Jacobians and eigenvalues

The convective flux Jacobian matrix with respect to the primitive variable vector (Q) is given as:

$$A = \frac{\partial F}{\partial Q} = \begin{pmatrix} V_n\rho_p & \rho n_x & \rho n_y & \rho n_z & \rho_{Y_v} V_n \\ uV_n\rho_p + n_x & \rho u n_x + \rho V_n & \rho u n_y & \rho u n_z & u\rho_{Y_v} V_n \\ vV_n\rho_p + n_y & \rho v n_x & \rho v n_y + \rho V_n & \rho v n_z & v\rho_{Y_v} V_n \\ wV_n\rho_p + n_z & \rho w n_x & \rho w n_y & \rho w n_z + \rho V_n & w\rho_{Y_v} V_n \\ Y_v V_n\rho_p & \rho V_n n_x & \rho V_n n_y & \rho V_n n_z & Y_v\rho_{Y_v} V_n + \rho V_n \end{pmatrix}. \tag{B.1}$$

The matrix A is evaluated at the cell face. n_x, n_y and n_z are the unit vectors along x, y and z axis respectively. The inverse of the time derivative matrix (Eq. (9)) is given as:

$$\Gamma^{-1} = \begin{pmatrix} \frac{\rho+\rho_{Y_v}Y_v}{\rho\rho_p} & 0 & 0 & 0 & -\frac{\rho_{Y_v}}{\rho\rho_p} \\ -\frac{u}{\rho} & \frac{1}{\rho} & 0 & 0 & 0 \\ -\frac{v}{\rho} & 0 & \frac{1}{\rho} & 0 & 0 \\ -\frac{w}{\rho} & 0 & 0 & \frac{1}{\rho} & 0 \\ -\frac{Y_v}{\rho} & 0 & 0 & 0 & \frac{1}{\rho} \end{pmatrix}. \tag{B.2}$$

Finally, the eigenvalues of the system of equation (Eq. (8)) can be obtained by computing the Jacobian:

$$A_\Gamma = \Gamma^{-1}A = \begin{pmatrix} V_n & \frac{\rho n_x}{\rho_p} & \frac{\rho n_y}{\rho_p} & \frac{\rho n_z}{\rho_p} & 0 \\ \frac{n_x}{\rho} & V_n & 0 & 0 & 0 \\ \frac{n_y}{\rho} & 0 & V_n & 0 & 0 \\ \frac{n_z}{\rho} & 0 & 0 & V_n & 0 \\ 0 & 0 & 0 & 0 & V_n \end{pmatrix}. \tag{B.3}$$

The eigenvalues of the matrix A_Γ are $\lambda_\Gamma = [V_n, V_n, V_n, V_n - c, V_n + c]$, where c is the speed of sound given by Eq. (A.1). When the preconditioning is used, ρ_p in the Γ^{-1} matrix is modified to ρ_p' to construct Γ_p^{-1} matrix. The rest of the elements of the Γ_p matrix are the same as Γ. Here, $\rho_p' = \frac{1}{U_\infty^2}$. The eigenvalues of the preconditioned system can by obtained by computing the modified flux Jacobian matrix given as:

$$A_{p\Gamma} = \Gamma_p^{-1}A = \begin{pmatrix} \frac{\rho_p}{\rho_p'}V_n & \frac{\rho n_x}{\rho_p} & \frac{\rho n_y}{\rho_p} & \frac{\rho n_z}{\rho_p} & 0 \\ \frac{n_x}{\rho} & V_n & 0 & 0 & 0 \\ \frac{n_y}{\rho} & 0 & V_n & 0 & 0 \\ \frac{n_z}{\rho} & 0 & 0 & V_n & 0 \\ 0 & 0 & 0 & 0 & V_n \end{pmatrix}. \tag{B.4}$$

The eigenvalues of the matrix A_{p_Γ} are $\lambda_{p\Gamma} = [V_n, V_n, V_n, \frac{1}{2}(V_n(1+\frac{c'^2}{c^2}) - \sqrt{V_n^2(1-\frac{c'^2}{c^2})^2 + 4c'^2}), \frac{1}{2}(V_n(1+\frac{c'^2}{c^2}) + \sqrt{V_n^2(1-\frac{c'^2}{c^2})^2 + 4c'^2})]$, where c' is the modified speed of sound based on $\rho_p' = \frac{1}{c'^2}$. Note that all the eigenvalues are of the order V_n; when $c'^2 = 1/\rho_p' = U_\infty^2$ is used for the preconditioning. When the physical-time derivative terms are treated in an implicit manner, they are combined with the preconditioned pseudo-time derivative terms. The resulting time derivative matrix inverse is given as:

$$\Gamma_{pi}^{-1} = \left(1 + \frac{3\Delta\tau}{2\Delta t}\right)^{-1} \begin{pmatrix} \frac{\rho+\rho_{Y_v}Y_v}{\rho\rho_p''} & 0 & 0 & 0 & -\frac{\rho_{Y_v}}{\rho\rho_p''} \\ -\frac{u}{\rho} & \frac{1}{\rho} & 0 & 0 & 0 \\ -\frac{v}{\rho} & 0 & \frac{1}{\rho} & 0 & 0 \\ -\frac{w}{\rho} & 0 & 0 & \frac{1}{\rho} & 0 \\ -\frac{Y_v}{\rho} & 0 & 0 & 0 & \frac{1}{\rho} \end{pmatrix}. \tag{B.5}$$

Here, $\rho_p'' = \frac{\rho_p' + \frac{3\Delta\tau}{2\Delta t}\rho_p}{1+\frac{3\Delta\tau}{2\Delta t}}$. Note that the eigenvalues of the corresponding flux Jacobian matrix ($A_{pi\Gamma} = \Gamma_{pi}^{-1}A$) are the same as $A_{p\Gamma}$.

References

Ahuja, V., Hosangadi, A., Arunajatesan, S., 2001. Simulations of cavitating flows using hybrid unstructured meshes. J. Fluids Eng. 123 (2), 331–340.

Bensow, R.E., Bark, G., 2010. Implicit LES predictions of the cavitating flow on a propeller. J. Fluids Eng. 132 (4), 1–10.

Bhatt, M., Mahesh, K., 2019. Investigation of propeller cavitation using compressible large eddy simulations. Sixth International Symposium on Marine Propulsors.

Bhatt, M., Mahesh, K., 2020. Numerical investigation of partial cavitation regimes over a wedge using large eddy simulations. Int. J. Multiph. Flow 122, 103155.

Boswell, R.J., 1971. Design, cavitation performance, and open-water performance of a series of research skewed propellers. Report. Naval Ship Research and Development Center Washington, D.C..

Brandao, F.L., Bhatt, M., Mahesh, K., 2020. Numerical study of cavitating regimes in flow over a circular cylinder. J. Fluid Mech. 885, A19.

Budich, B., Schmidt, S., Adams, N., 2018. Numerical simulation and analysis of condensation shocks in cavitating flows. J. Fluid Mech. 838, 759–813.

Colonius, T., 2004. Modeling artificial boundary conditions for compressible flow. Annu. Rev. Fluid Mech. 36, 315–345.

Franc, J.-P., Michel, J.-M., 2006. Fundamentals of Cavitation, 76. Springer Science & Business Media.

Ganesh, H., Makiharju, S.A., Ceccio, S.L., 2016. Bubbly shock propagation as a mechanism for sheet-to-cloud transition of partial cavities. J. Fluid Mech. 802, 37–78.

Gnanaskandan, A., 2015. Development of a methodology for LES of turbulent cavitating flows.

Gnanaskandan, A., Mahesh, K., 2015. A numerical method to simulate turbulent cavitating flows. Int. J. Multiph. Flow 70, 22–34.

Gnanaskandan, A., Mahesh, K., 2016. Large eddy simulation of the transition from sheet to cloud cavitation over a wedge. Int. J. Multiph. Flow 83, 86–102.

Gnanaskandan, A., Mahesh, K., 2016. Numerical investigation of near-wake characteristics of cavitating flow over a circular cylinder. J. Fluid Mech. 790, 453–491.

Guillard, H., Viozat, C., 1999. On the behavior of upwind schemes in the low Mach number limit. Comput. Fluids 28 (1), 63–86.

Hou, Y., Mahesh, K., 2005. A robust, colocated, implicit algorithm for direct numerical simulation of compressible, turbulent flows. J. Comput. Phys. 205 (1), 205–221.

Hsiao, C.-T., Chahine, G.L., 2005. Scaling of tip vortex cavitation inception noise with a bubble dynamics model accounting for nuclei size distribution.. J. Fluids Eng. 127 (1), 55–65.

Hsu, J., Jameson, A., 2002. An implicit-explicit hybrid scheme for calculating complex unsteady flows. In: 40th AIAA Aerospace Science Meeting & Exhibit, p. 714.

Jameson, A., 1995. Analysis and design of numerical schemes for gas dynamics, 1: artificial diffusion, upwind biasing, limiters and their effect on accuracy and multigrid convergence. Int. J. Comput. Fluid Dyn. 4 (3-4), 171–218.

Karplus, H.B., 1957. Velocity of sound in a liquid containing gas bubbles. J. Acoust. Soc. Am. 29, 12–61.

Kunz, R.F., Boger, D.A., Stinebring, D.R., Chyczewski, T.S., Lindau, J.W., Gibeling, H.J., Venkateswaran, S., Govindan, T.R., 2000. A preconditioned Navier–Stokes method for two–phase flows with application to cavitation prediction. Comput. Fluids 29 (8), 849–875.

LeMartelot, S., Nkonga, B., Saurel, R., 2013. Liquid and liquid-gas flows at all speeds. J. Comput. Phys. 255, 53–82.

Li, X.S., Gu, C., 2008. An all-speed Roe-type scheme and its asymptotic analysis of low Mach number behavior. J. Comput. Phys. 227 (10), 5144–5159.

Lindau, J., Kunz, R., Venkateswaran, S., Merkle, C., 2001. Development of a fully-compressible multi-phase Reynolds-averaged Navier–Stokes model. In: 15th AIAA Computational Fluid Dynamics Conference, p. 2648.

Liu, T.G., Khoo, B.C., Xie, W.F., 2004. Isentropic one–fluid modeling of unsteady cavitating flow. J. Comput. Phys. 201 (1), 80–108.

Mahesh, K., Constantinescu, G., Moin, P., 2004. A numerical method for large eddy simulation in complex geometries. J. Comput. Phys. 197 (1), 215–240.

Merkle, C.L., 1998. Computational modelling of the dynamics of sheet cavitation. 3rd International Symposium on Cavitation, Grenoble, France.

Moin, P., Squires, K., Cabot, W., Lele, S., 1991. A dynamic subgrid-scale model for compressible turbulence and scalar transport. Phys. Fluids 3(11), 2746–2757.

Park, N., Mahesh, K., 2007. Numerical and modeling issues in LES of compressible turbulence on unstructured grids. In: Proceedings of the 45th AIAA Aerospace Sciences Meeting and Exhibit, AIAA Paper, pp. 1–18.

Saito, Y., Takami, R., Nakamori, I., Ikohagi, T., 2007. Numerical analysis of unsteady behavior of cloud cavitation around a NACA0015 foil. Comput. Mech. 40 (1), 85–96.
Schnerr, G.H., Sezal, I.H., Schmidt, S.J., 2008. Numerical investigation of three-dimensional cloud cavitation with special emphasis on collapse induced shock dynamics. Phys. Fluids 20 (4), 1–9.
Senocak, I., Shyy, W., 2002. A pressure–based method for turbulent cavitating flow computations. J. Comput. Phys. 176 (2), 363–383.
Seo, J.H., Lele, S., 2009. Numerical investigation of cloud cavitation and cavitation noise on a hydrofoil section. In: 7th International Symposium on Cavitation, pp. 1–15.
Singhal, A.K., Athavale, M.M., Li, H., Jiang, Y., 2002. Mathematical basis and validation of the full cavitation model. J. Fluids Eng. 124 (3), 617–624.
Turkel, E., 1999. Preconditioning techniques in computational fluid dynamics. Annu. Rev. Fluid Mech. 31, 385–416.
Vatsa, V., Turkel, E., 2003. Choice of variables and preconditioning for time dependent problems. In: 16th AIAA Computational Fluid Dynamics Conference, p. 3692.
Venkateswaran, S., Lindau, J.W., Kunz, R.F., Merkle, C.L., 2002. Computation of multiphase mixture flows with compressibility effects. J. Comput. Phys. 180 (1), 54–77.
Venning, J.A., Khoo, M.T., Pearce, B.W., Brandner, P.A., 2018. Background nuclei measurements and implications for cavitation inception in hydrodynamic test facilities. Exp. Fluids 59, 71.
Weiss, J.M., Smith, W.A., 1995. Preconditioning applied to variable and constant density flows. J. Comput. Phys. 33 (11), 2050–2057.
Williamson, C.H.K., 1996. Vortex dynamics in the cylinder wake. Annu. Rev. Fluid Mech. 28, 477–539.
Yee, H.C., Sandham, N.D., Djomehri, M.J., 1999. Low-dissipative high-order shock–capturing methods using characteristic-based filters. J. Comput. Phys. 150 (1), 199–238.